DESCRIPTION AND PERFORMANCE OF MEA, THE MAGNETIC DETECTOR AT ADONE

W. W. ASH[1], D. C. CHENG[2], B. ESPOSITO, F. FELICETTI, A. MARINI,
H. OGREN[3], I. PERUZZI, M. PICCOLO, F. RONGA, G. SACERDOTI

Laboratori Nazionali di Frascati, Frascati, Italy

L. TRASATTI[4], G. T. ZORN

Dept. of Physics and Astronomy, University of Maryland, College Park, Maryland 20742, U.S.A.[5]

B. BARTOLI, B. COLUZZI, A. NIGRO, V. SILVESTRINI, F. VANOLI

Istituto di Fisica dell'Università di Napoli, and Istituto Nazionale di Fisica Nucleare, Sezione di Napoli, Italy

D. BISELLO, A. MULACHIÉ, M. NIGRO, L. PESCARA, R. SANTANGELO[6], E. SCHIAVUTA

Istituto di Fisica dell'Università di Padova, and Istituto Nazionale di Fisica Nucleare, Sezione di Padova, Italy

D. SCANNICCHIO

Istituto di Fisica dell'Università di Pavia, and Istituto Nazionale di Fisica Nucleare, Sezione di Pavia, Italy

P. MONACELLI, L. PAOLUZI, G. PIANO-MORTARI and F. SEBASTIANI

Istituto di Fisica dell'Università di Roma, and Istituto Nazionale di Fisica Nucleare, Sezione di Roma, Italy

The experimental detector at Adone, MEA, which operates with its magnetic field perpendicular to the e^+e^- beams is described. Studies of the magnetic compensation for operation at Adone and resulting magnetic fields are presented. Particles are detected and analyzed using narrow-gap and wide-gap spark chambers which are triggered by scintillation and proportional counters. Momentum measurements for charged particles are made with $\Delta p/p = \pm 0.07$ at $p = 1$ GeV/c ($B = 2.5$ kG) and angles are measured to better than $\pm 1.5°$ over a solid angle of $\sim 0.3 \times 4\pi$ sr.

1. Introduction and general description

MEA, Magnet for Experiments at Adone, is a detector system developed at Frascati to investigate e^+e^- interactions in the center-of-mass energy interval $\sqrt{s} = 1.2$–3.0 GeV produced at Adone[1]).

A photograph of MEA taken during its installation at Adone is shown in fig. 1. In fig. 2 a drawing of the MEA magnet is seen along with the coordinate system and the angles to be used later in its description. A cross section through the e^+e^- beam line of the spectrometer system is shown in fig. 3. This figure shows the magnet compensators and the complete particle detection system.

As seen in figs. 2 and 3 the solenoidal magnet system was mounted with its axis perpendicular to the Adone straight section with the compensation magnets for this transverse field placed just inside the magnet coil. The choice of this geometry was imposed by the particular space limitations at Adone coupled with the optical read-out requirements. Although the arrangement having the magnetic field axis along the beam line is now in more common use in colliding beam experiments, we chose optical chambers with the advantages they have in the analysis of unusual and unexpected events.

The detection system shown in fig. 3 uses optical spark chambers and scintillation counters located both inside and outside the main coil as well as multiwire proportional chambers (MWPC) near the e^+e^- interaction region. The scintillators and MWPC are used to trigger the spark chamber system. Cosmic-ray triggers were suppressed by particle and bunch–bunch timing measurements and by source definition using the fast logic of the MWPC. This detection system measures the mo-

---
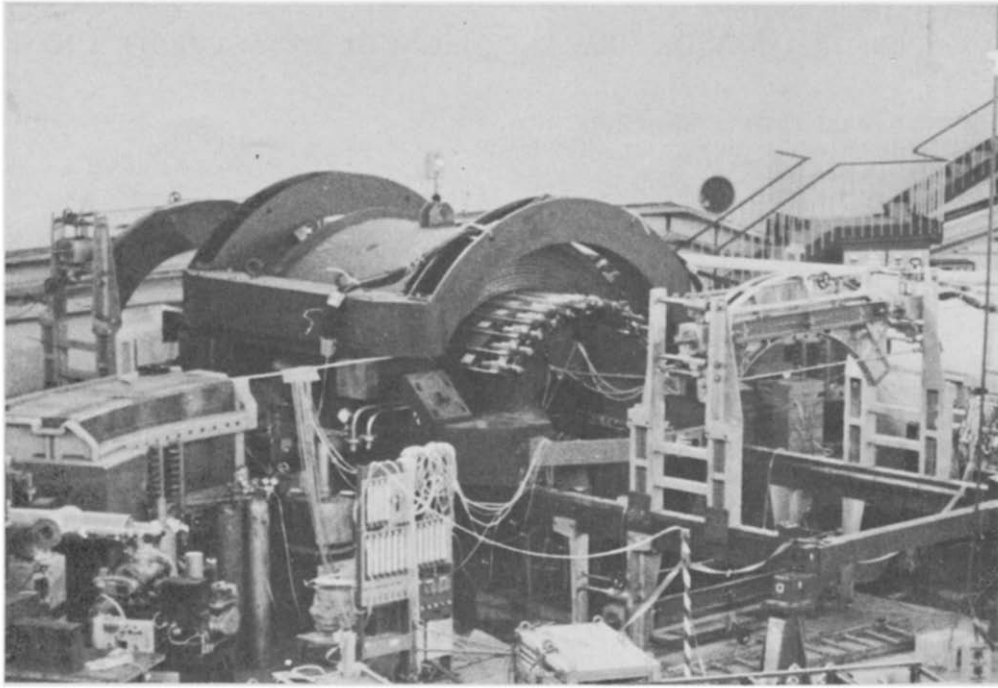
Fig. 1. Photograph of MEA during installation at Adone.
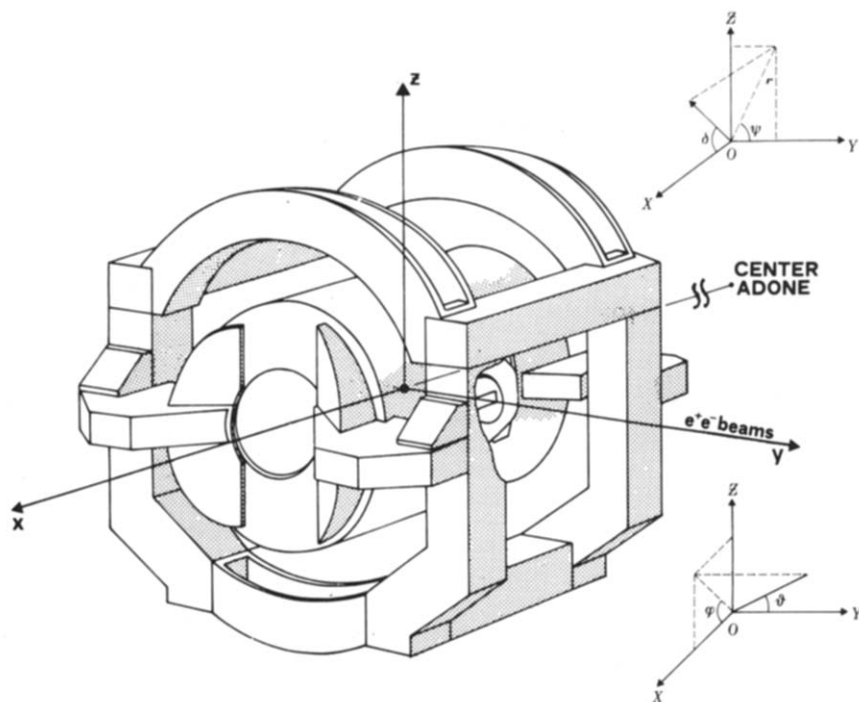
Fig. 2. MEA solenoid with the front iron plates connected to lateral bars for flux return. Also shown are the coordinate system and angles used in description of apparatus.
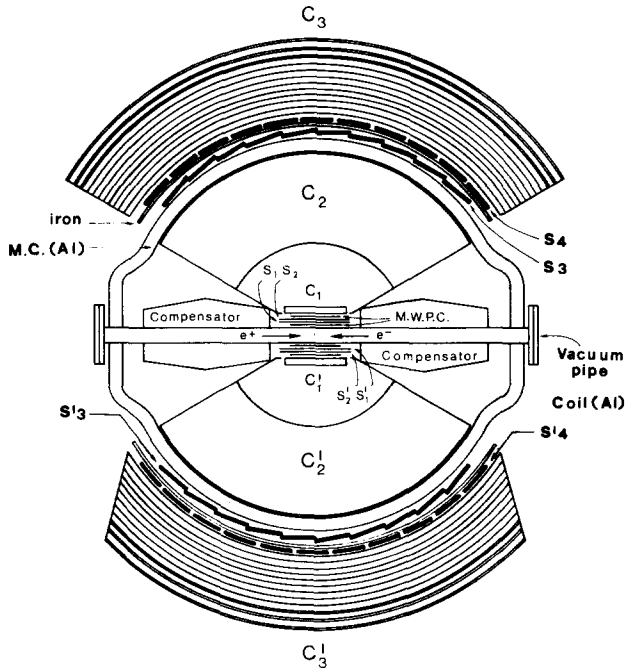
Fig. 3. Vertical section through the experimental apparatus: C_1 C_1' narrow-gap spark chambers; C_2 C_2' wide gap cylindrical spark chambers; C_3 C_3' thick-plate spark chambers for particle identification; MWPC multiwire proportional chambers; $S_1, ..., S_4'$ scintillation counters for triggering the apparatus.

menta of charged particles produced in the e^+e^- collisions at Adone and gives some informations on the identity of both charged particles and gamma rays.

In this report we will describe the experimental details of the apparatus and its performance. In section 2 the magnetic compensation necessary at Adone for the transverse magnetic field of MEA is discussed and the characteristics of the main MEA field are given. In section 3 a description of each of the principal element comprising the detection system is given. Finally, the performances of the detector as a spectrometer is presented in section 4.

2. Properties of the magnetic field of MEA and its interaction with Adone

The magnet system shown in fig. 2 with its 2 m diameter by 2 m long coils produces a maximum magnetic field of 4.5 kG. The maximum field used during operation at Adone was 3.0 kG (see sect. 3.5.2). The characteristics of the main magnet and magnetic compensators are presented in table 1. The main magnet coils and compensators are powered in series. Small field correction coils with

TABLE 1

MEA magnet characteristics.

Main magnet
  Max. magnetic field 4.5 kG at 4.5 kA (max. power 1.3 MW)
  Coil dimensions: length 2.0 m, coil inside diam. 1.94 m
  Al coil, 180 turns in 2 layers, cond. 3.4×2.1 cm^2, with 9 mm diam. hole
  Magnetic flux return, $4-45 \times 45$ cm^2 Fe bars
  Weight 82 t

Compensation magnet (two required)
  Max. magnetic field 4.5 kG at 4.5 kA (max. power 0.35 MW)
  Max. magnetic field in Fe 18 kG
  Outside dimensions: length 0.74 m, width 0.6 m, height 0.4 m
  Cu coils, 1.1×1.1 cm^2 with 6 mm diam. hole
  Weight 350 Kg

a separate power supply are used to tune this compensation system to permit operations at all useful magnet currents up to the maximum value.

2.1. MAGNETIC COMPENSATION FOR MEA

The magnetic system that was used to compensate for the deflection of the e^-e^+ beams at Adone, has two compensating magnets placed inside MEA along the beam lines (see fig. 3). The central region is left clear for the detection of e^+e^- interactions. Fig. 4 shows a section of the main compensation magnets, perpendicular to the e^+e^- beams. These compensators generate field opposite in direction to the main field over $\sim 50\%$
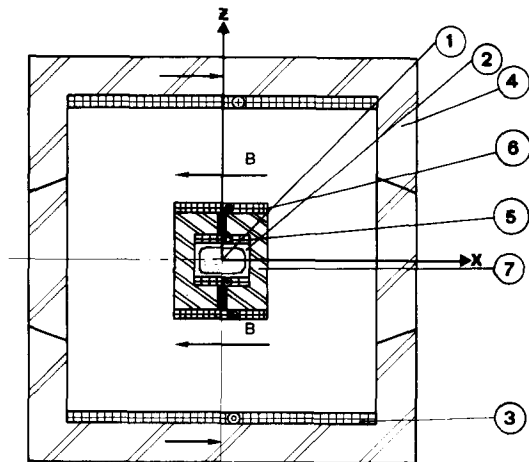
Fig. 4. Schematic drawing of the magnetic system (solenoid and compensators). (1) e^+e^- beams; (2) Adone vacuum pipe; (3) main magnet coils; (4) flux return iron; (5) compensating winding N1 and correction coil; (6) compensating winding N2; (7) compensator iron.
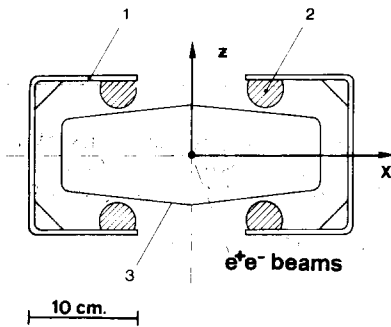
Fig. 5. Soft iron inserts for compensator magnets to correct for sextupole term of compensator magnetic field. (1) Aluminium support; (2) one of four soft-iron cylinders; (3) Adone vacuum chamber.

of the beam line through MEA. Coils N_2 and the internal iron-yoke pieces shown in fig. 4, minimize the non-uniformity of the field produced by the insertion of the compensators and produce a zero field cavity along the e^+e^- beams. Coil N_1 is in this cavity and the field it produces is uniform. A further addition was made to the magnetic system of four soft iron bars placed inside each compensator, as shown in fig. 5. These were used to compensate for the sextupole field generated by the compensators.

The interaction of this compensation system with e^+e^- beams at Adone will now be considered. In order for it to have a negligible effect on the stability of the stored beams, two basic conditions on the transverse magnetic field, B_x, must be satisfied by the system,

$$B_x(x, y, z) = B_x(x, -y, z), \tag{1}$$

$$\int B_x(x, y, z)\, \mathrm{d}y = 0, \tag{2}$$

where y is a coordinate measured from the center of the magnet along the ideal beam orbit (see fig. 2).

Condition (1) is necessary to insure that, even when eq. (2) is satisfied, there will be no net beam displacement. Condition (2) implies that there is no net change in angle of the beams passing through the system. Both conditions must be satisfied not only along the beam axis, but also for vertical and horizontal displacements of ± 2 cm from this axis. Deviation from condition (2) can be written as a function of the displacement in x and z in the following form:

$$\int B_x(x, y, 0)\, \mathrm{d}y = -(A + Bx - Cx^2 - Dx^3 + Ex^4 + \ldots),$$

$$\int B_x(0, y, z)\, \mathrm{d}y \tag{3}$$

$$= -(A + B'z + Cz^2 + D'z^3 + Ez^4 + \ldots).$$

These expressions were derived using Maxwell's equations and condition (1). The maximum absolute values at Adone[2]) are partially summarized in table 2. The value of $A \lesssim 2.5$ G·m is given by restricting the maximum displacement from the equilibrium orbit anywhere in the machine to 2 mm. The values $B, B' \lesssim 0.7$ G·m/cm results from the requirement that $\Delta v/v_0$, the fractional

TABLE 2

Multipole expansion coefficients for the MEA magnetic field along the e^+e^- beam line.

	MEA magnet current (A)	B (G·m/cm)	B' (G·m/cm)	C (G·m/cm^2)	E (G·m/cm^4)
Max. allowed values	–	0.70	0.70	0.70	
Experimentally measured values	2000	−0.42 ±0.14	0.03 ±0.12	−0.79 ±0.12	0.08 ±0.03
	3000	−0.55 ±0.12	0.01 ±0.10	−1.08 ±0.11	0.10 ±0.03
	4000	−0.65 ±0.14	0.64 ±0.13	−0.09 ±0.13	0.18 ±0.02
	4200	−0.23 ±0.32	0.78 ±0.19	0.06 ±0.54	0.19 ±0.07

betatron number shift in horizontal and vertical planes, be less than 10^{-3}. The limit of $C \lesssim 0.7$ G·m/cm^2 specifies that the sextupole term introduced by the MEA system be less than 20% of the integrated sextupole term of Adone. Similarly $D, D' \lesssim 1.0$ G·m/cm^3 specifies that the octupole component does not exceed the octupole term already present in Adone.

In the measurements that were made of the coefficients of the expansion of eq. (3), the symmetry of the magnetic field along y allowed us to ignore odd powered terms greater than first order. As the coefficients of even powered terms were found to be quite small above fourth order, they also were ignored. Since the active length of the beam magnet interaction is about 3 m, the above stated condition on the value of A implies an absolute measurement of B_x to better than ± 0.8 G over the entire range -4500 G to $+4500$ G and a relative precision of ± 0.2 G for displacements off-axis.

The field integral was determined by measuring the force on a current carrying rod[3-5]). The absolute precision of the measurement was better than
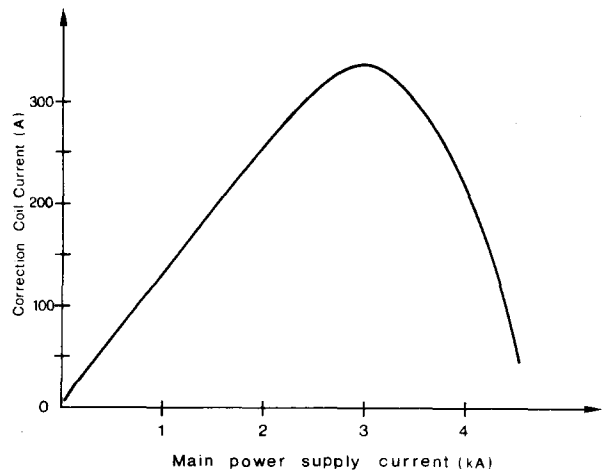
Fig. 6. Compensator correction-coil power-supply current required to give zero field integral, plotted vs main power-supply current.

± 0.5 G·m. The position of the rod was determined by an optical survey to ± 1 mm. The main coil and the compensator coils were connected in series electrically, so apart from small design errors and effects of saturation, the field integral was ex-
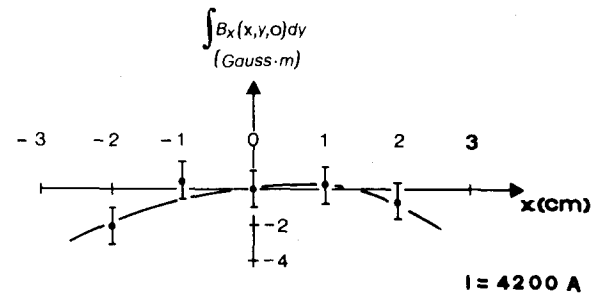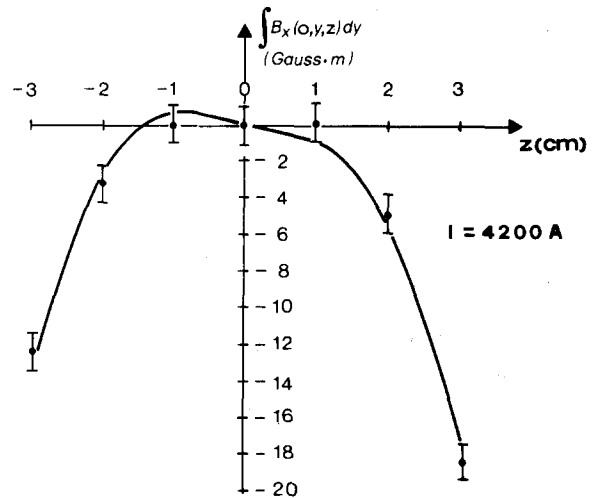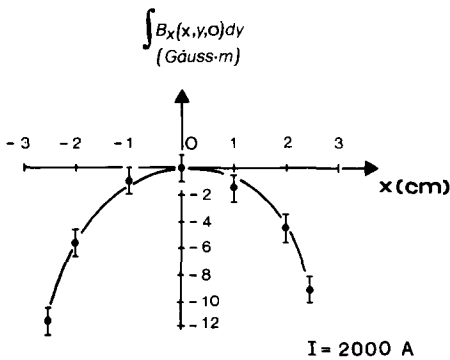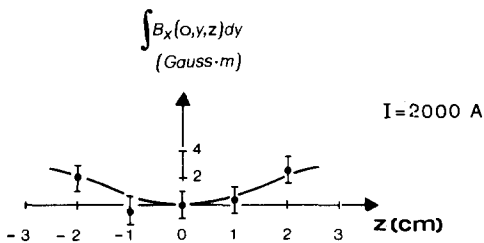
Fig. 7. Measurements of the integral of B_x along y for displacement in x and z at $I = 2.0$ and 4.2 kA. Coordinate system is that shown in fig. 2.

pected to be near zero for all values of the main current.

The integral term A along the equilibrium orbit was zeroed over the entire range 0–4500 A using a correction coil (see fig. 4). Fig. 6 shows the correction coil current as a function of the main current. The reproducibility of all points was $\lesssim 0.5\%$ and the sensitivity was 0.3 G·m/A for the main coil and 1.6×10^{-3} G·m/mA for the correction coil. The simplicity of this corrections system greatly eased the problems associated with operations at Adone.

Fig. 7 shows the results of the measurements of $\int B_x(x, y, 0)dy$ and $\int B_x(0, y, z)dy$ for two values of the magnet current. Also indicated in the figure are the multipole expansion curves fitted to these points. The maximum calculated values and those measured experimentally are given in table 2. As can be seen the measurements satisfy these maximum limits with one possible exception of a single value for C.

In fig. 8 a profile of B_x along the beam is shown at 4500 A. From these measurements, the electron trajectory shown in the same figure was calculated. The central vertical displacement, at 4500 A ranges from 18 mm to 6 mm with the mo-

mentum of the electron ranging from 500 MeV/c to 1500 MeV/c. These displacements are quite compatible with the vertical height of the vacuum chamber of 40 mm.

With this compensation system MEA has successfully operated at Adone at all e^+e^- beam energies.

2.2. MEA FIELD MAP

Momentum analysis of events require a precise determination of field components at all points inside the detection volume of the solenoid.

The field was mapped using a self-propelled Hall-probe measuring head whose coordinates and associated field component values were simultaneously read out by a PDP-8 computer and recorded on magnetic tape[4,5]. The measuring head carried three orthogonal Hall probes and mapped the field components B_x, B_ψ, B_r in a cylindrically symmetric system around the solenoidal axis (x) (see fig. 2). All the measurements were made with the compensators operating to give a zero field integral. Fig. 9 shows the principal projections of the field map at 4500 A. B_x is uniform within 15% for $r = 0.5$–1.0 m, while for small x and for small r where the influence of the compensators is strong-
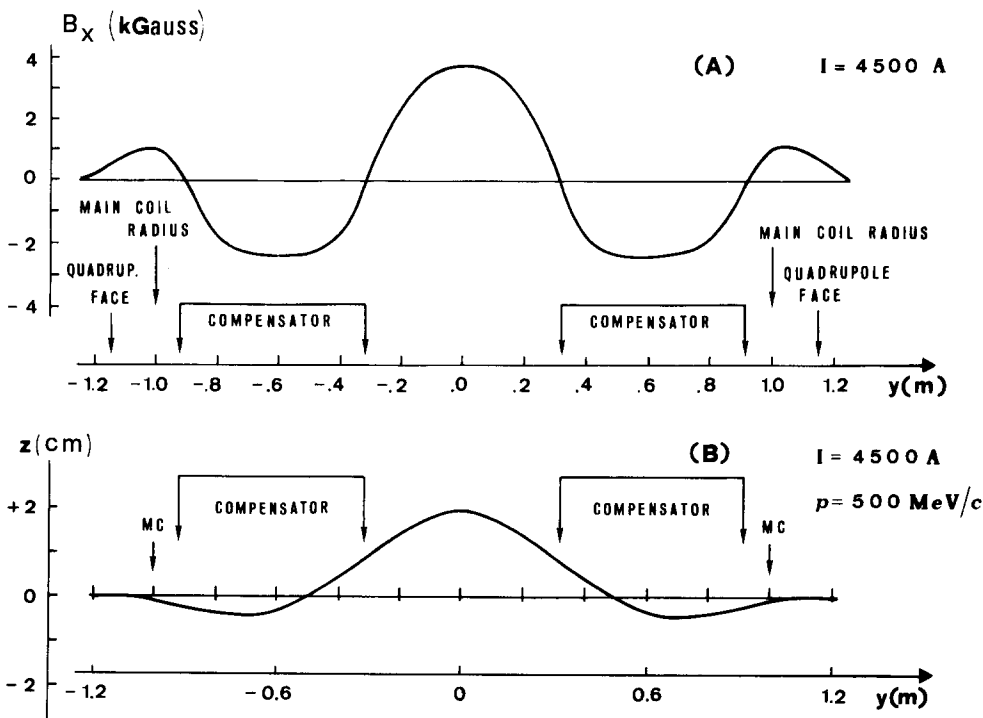
Fig. 8. At the maximum current 4.5 kA: (A) B_x vs y, and (B) the electron path in the vertical plane (y–z) for a momentum $p = 500$ MeV/c.
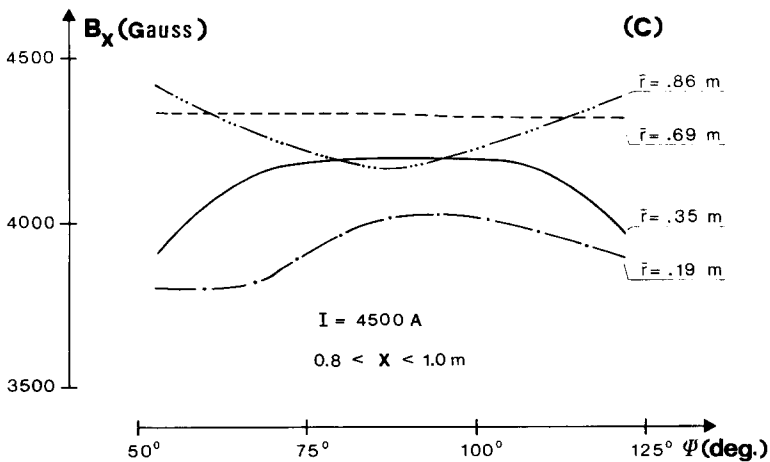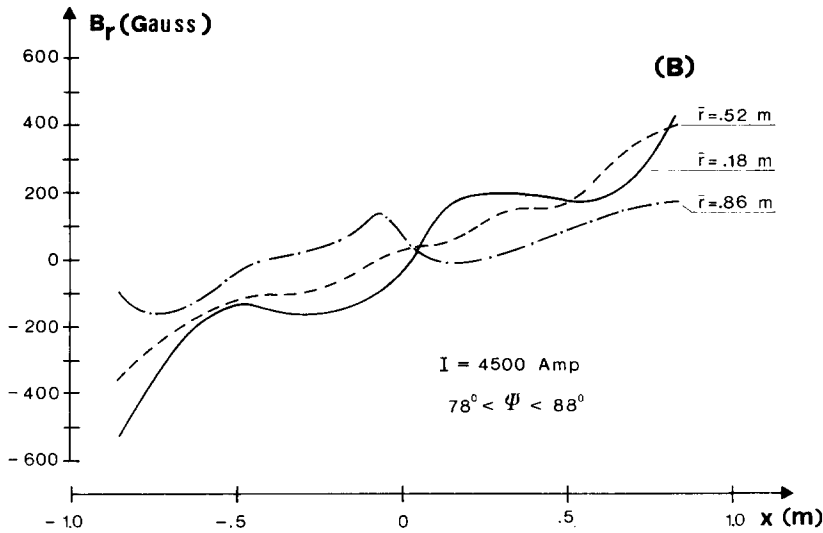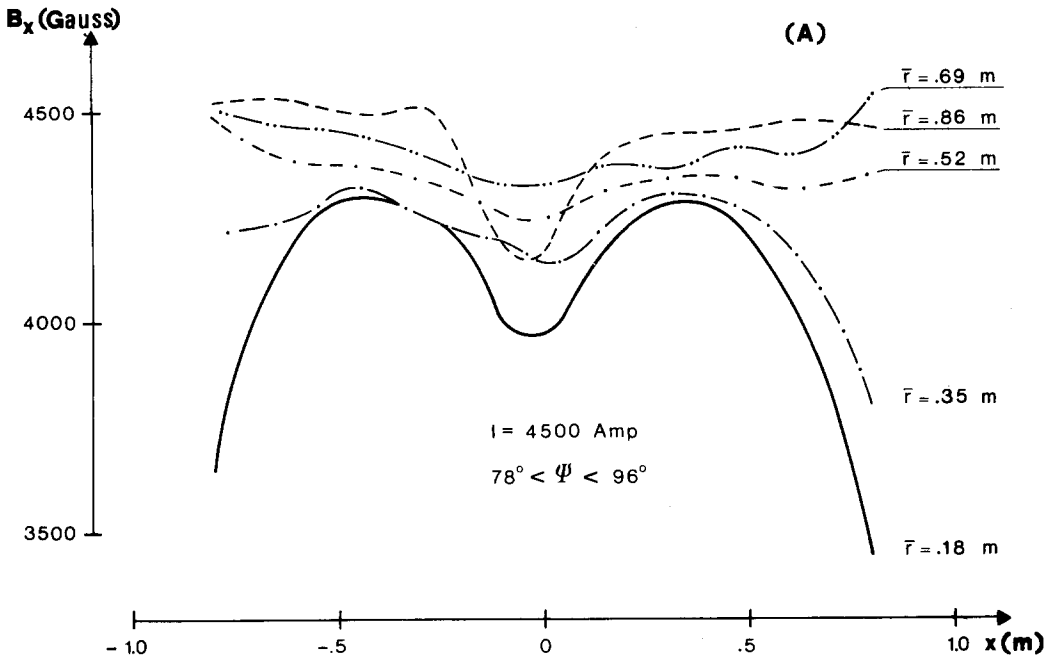
Fig. 9. (A) B_x vs x for $(78° < \psi < 96°)$ and for 5 average values of r, (B) B_r vs x for $(78° < \psi < 88°)$ and for 3 average values of r, and (C) B_x vs ψ for $(0.8 < x < 1$ m) and for 4 average values of r.

er, there is a reduction in the field of up to 30%. Field uniformity in ψ is very good, better than 2% except for points very near the compensators.

An analytic fit to the measured field components was obtained taking into account explicitly the compensator fringing fields, the small gap in the main field winding were the two halves of the coil join, and the two large holes in the iron end caps (see figs. 2 and 4). This was accomplished by first expressing each field component in the form $(1+x+x^2)(1+r^2)(1+\cos^2\psi)$ and then by adding dipole fields to simulate effect of the compensators. In addition three current loops were added: one in the central plane to simulate a missing winding between the halves of the main coil, and two at both ends for the holes in the end caps. In these cases the currents were individually adjustable. This fitting procedure was restricted to the detection region. For the principal component B_x in this region an average fitting error of $\pm 0.3\%$ was obtained. This value represents a maximum for the momentum reconstruction error due to the magnetic field uncertainty and is well below estimated uncertainties due to errors in event measurements on the film (see section 4).

3. Description of detection system

3.1. INTERNAL SPARK-CHAMBER SYSTEM (ISC)

The ISC includes two wide-gap chambers and two thin-gap chambers placed above and below the interaction region. The arrangement is shown in fig. 3. The physical characteristics of these chambers are summarized in table 3 and fig. 10.

The two large wide-gap chambers (C_2, C_2' of fig. 3) have transparent wire electrodes and are used to measure the outgoing particle momenta. Each chamber has four gaps. Wire electrodes were used in order to allow the viewing of sparks through the electrodes themselves. This was necessary as the end plates of the central magnetic return yoke do not permit the chambers to be viewed through their plexiglass ends. With this arrangement however, the complete spatial reconstruction of visable tracks is possible using one view only. See section 4 for a description of the spatial reconstruction method used.

A schematic drawing of one of these chambers is shown in fig. 11. Each wire electrode is made of a separate layer of wires 100 μm in diameter. Adjacent electrodes are spaced a distance of 2.5 cm. This double layer decouples the gaps and was found to be essential for the satisfactory operation of these chambers[6]. The separation of electrodes also made spatial reconstruction easier as the end points of each track are then separated in space and can be more easily seen and measured. A further improvement was made in order to achieve good working conditions, namely, 15 equispaced guard wires were placed in each gap at the ends of each chamber. These were connected to the plates through a resistor chain so that when the hv pulse was applied to the chamber, the electric field near the edges was approximately equal to the field inside the gaps. In order to be able to work with good efficiency even with a rather low electric field (~ 6 kV/cm) the gas mixture of Neogal 90 (90% neon; 10% helium) was used. Spu-
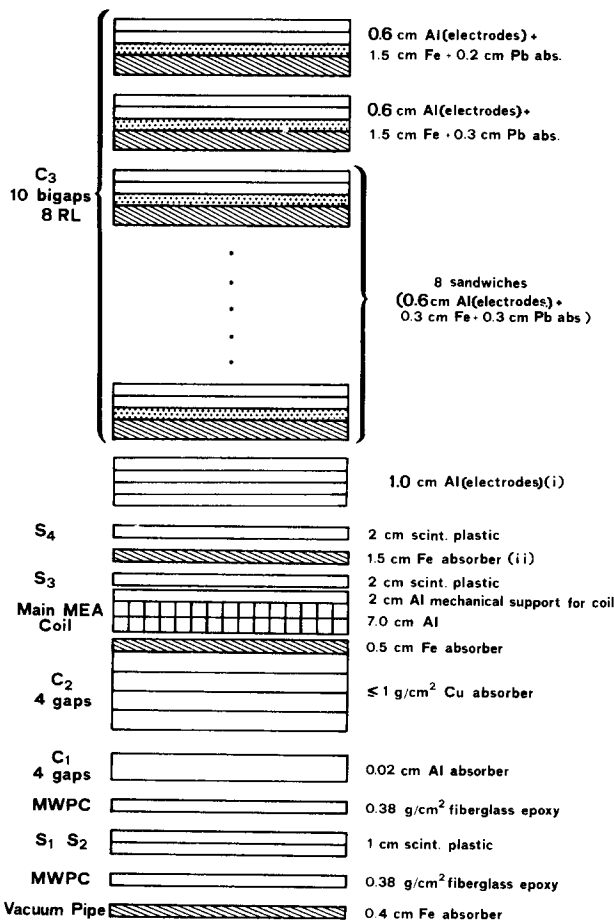
Fig. 10. Absorber thickness of vacuum pipe, MWPC, internal spark chambers (C_1, C_2) and external spark chamber (C_3) for the upper part of apparatus. The lower part of apparatus with chambers C_1' C_2' was identical except that the chamber indicated with (i) was removed and the absorber (ii) was replaced with 0.5 cm Pb.

Labels in figure:

C_3 10 bigaps 8 RL

0.6 cm Al(electrodes) + 1.5 cm Fe · 0.2 cm Pb abs.

0.6 cm Al(electrodes)+ 1.5 cm Fe · 0.3 cm Pb abs.

8 sandwiches (0.6cm Al(electrodes) + 0.3 cm Fe · 0.3 cm Pb abs)

1.0 cm Al(electrodes)(i)

S_4 — 2 cm scint. plastic
1.5 cm Fe absorber (ii)
S_3 — 2 cm scint. plastic
Main MEA Coil — 2 cm Al mechanical support for coil
7.0 cm Al
0.5 cm Fe absorber
C_2 4 gaps — $\leqslant 1$ g/cm^2 Cu absorber
C_1 4 gaps — 0.02 cm Al absorber
MWPC — 0.38 g/cm^2 fiberglass epoxy
S_1 S_2 — 1 cm scint. plastic
MWPC — 0.38 g/cm^2 fiberglass epoxy
Vacuum Pipe — 0.4 cm Fe absorber

TABLE 3

Characteristics of internal spark chambers and MWPCs[a].

	Narrow-gap spark chambers $C_1 C_1'$	Cylindrical wide-gap chambers $C_2 C_2'$	Multiwire proportional chambers MWPC
Description	4–8 mm gaps 59.6×43.8× 5.4 cm³, Al foil plates, 11.0– 15.6 cm from e+e− beams, voltage 10 kV, gas Henogal 30	4–10 cm gaps, 100 μm wires, 0.25 cm spacing, plate radii 50.5–98.0 cm, length 184 cm, elec. field ~6 kV/cm, gas Henogal 90	Two 24.5×36.2×1.4 cm³, 98 20 μm sense wires, 0.254 cm spacing, 6 cm from e+e− beams
			Two 39.0×36.2×1.4 cm³, 154 20 μm sense wires, 0.254 cm spacing, 10.5 cm from e+e− beams
			Voltage 4.7 kV, gas "magic"
Geometric angular acceptance (from point source to mid-chamber)	$25° \leqslant \delta \leqslant 155° (\psi = \pm 90°)$ $40° \leqslant \psi \leqslant 140° (\delta = \pm 90°)$	$50° \leqslant \delta \leqslant 130° (\psi = \pm 90°)$ $38° \leqslant \psi \leqslant 142° (\delta = \pm 90°)$	$25° \leqslant \delta \leqslant 155° (\psi = \pm 90°)$ $30° \leqslant \psi \leqslant 150° (\delta = \pm 90°)$

[a] For absorber thicknesses see fig. 10.
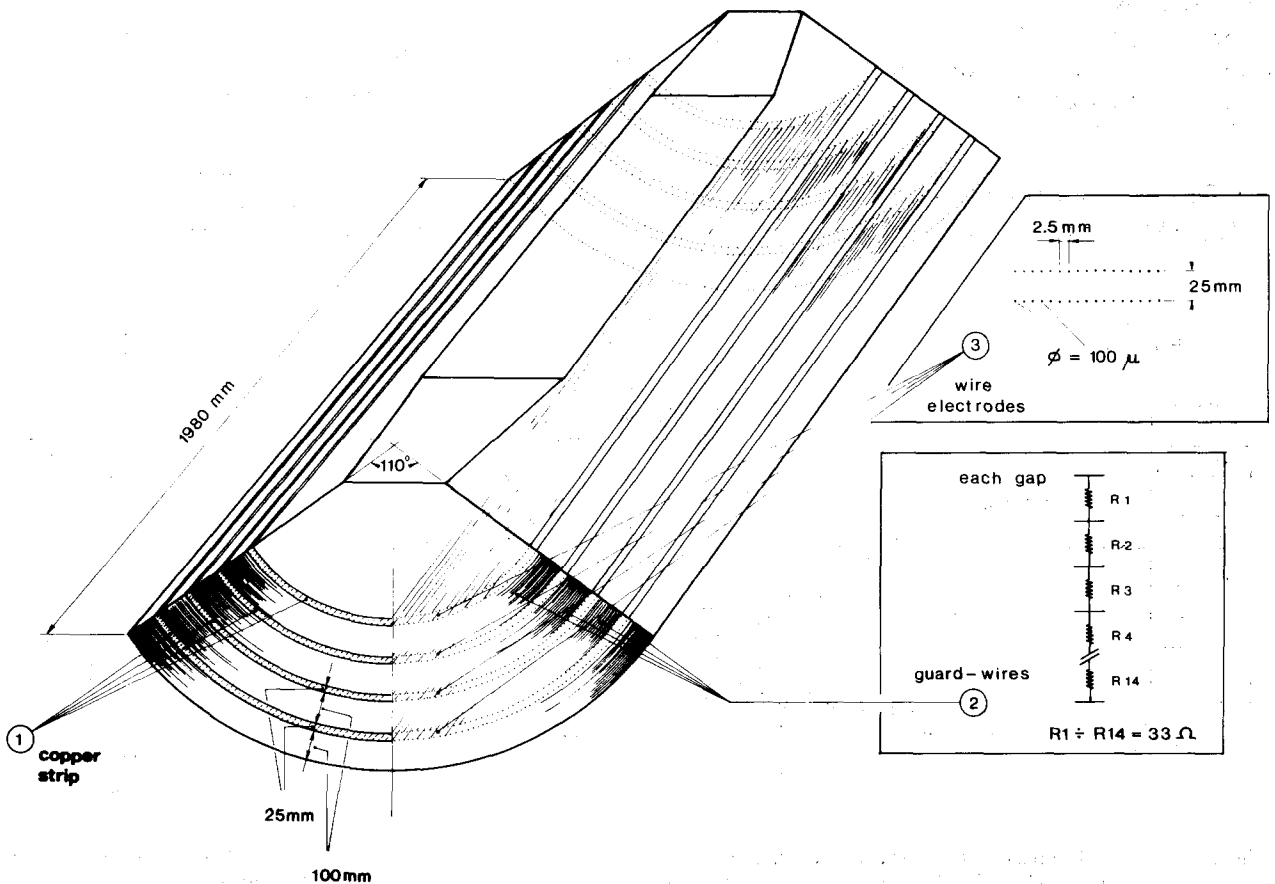
Fig. 11. Schematic view of a cylindrical wide-gap spark chamber.

rious tracks and sparks were suppressed by the addition of ~10% (by volume) of ethyl-alcohol vapor.

The applied hv pulse is generated by a 4-stage Marx generator with output capacity $C = 3800$ pF. The rise time of this pulse is about 50 ns, much longer than the transmission time of the chamber. The characteristic impedance of the chamber is 40 Ω. A resistance of 50 Ω in parallel with each chamber increased the pulse rise time and was found to reduce the fluctuations in track brightness. With the electric field of 6 kV/cm the efficiency for registration of track having small angles relative to the electric field ξ, was ~100% for each gap. The efficiency was high out to angles of $\xi = 40°$. At greater angles the sparks became less bright and eventually vanished. For more detailed information on the development and testing of these chambers see ref. 6, 7 and 8.

Below and above the vacuum pipe two small plane-plate spark chambers (C_1, C_1' in fig. 3) each with four 8 mm gaps are used to measure particle trajectories close to the interaction region. These chambers are pulsed with a 10 kV pulse from a central spark-gap pulser through cables to each bigap. The recovery time for the ISC system is ~0.5 s.

3.2. THE EXTERNAL SPARK-CHAMBER SYSTEM (ESC)

The ESC consist of four heavy-plate cylindrical spark chambers covering most of the main coil of the magnet (C_3, C_3' in fig. 3). As seen in fig. 12, two chambers were placed above the magnet coil and two below. These chambers were designed for gamma-ray and electron detection, pion–muon discrimination, and range analysis for intermediate energy particles. Each chamber has ~8 radiation lengths or ~0.8 collisions lengths. [The total material thickness following spark chambers $C_2(C_2')$ including $C_3(C_3')$, is 10.4 radiation or 1.4 collision lengths.] The physical characteristics of these chambers are presented in table 4 and in fig. 10.

TABLE 4

Characteristics of external spark chambers[a].

	Cylindrical spark chambers $C_3 C_3'$
Description	Four 10 bigap cylindrical spark chambers, radii 1.12–1.74 m, length 1.0 m, small-angle mirrors at one end, voltage 11 kV, gas Henogal 30[b]
Geometrical angular acceptance (point source to midchamber)	$53° \leqslant \delta \leqslant 127°$ for $C_3 C_3'$ ($\psi = \pm 90°$) $36° \leqslant \psi \leqslant 144°$ for C_3 ($\delta = \pm 90°$) $48° \leqslant \psi \leqslant 132°$ for C_3' ($\delta = \pm 90°$)

[a] For details on absorber thicknesses see fig. 10.
[b] An additional quadrigap chamber was inserted in C_3'.
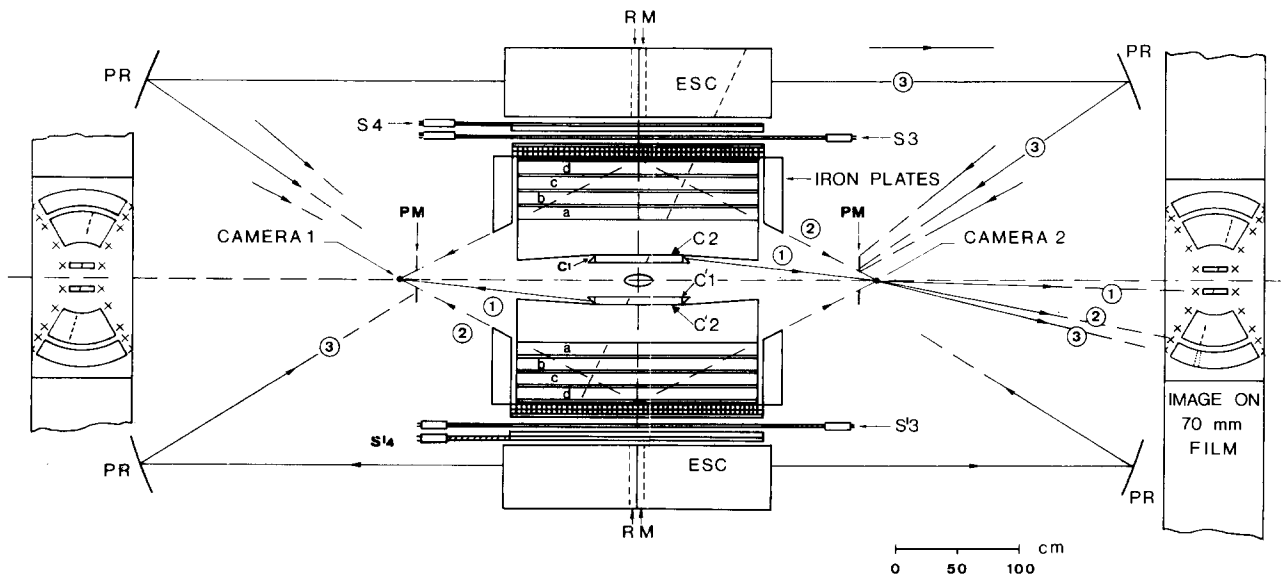
Fig. 12. Drawing of optical system used in photography of MEA spark-chamber system. The narrow-gap spark chambers (C_1 C_1') and the wide-gap chambers (C_2 C_2') are seen directly by two cameras; the external spark chambers are imaged on same film through the parabolic mirrors PR, and the plane mirrors, PM.

A rough estimate of the photon detection efficiency for the ESC was obtained from measurements made with monoenergetic photons incident on an absorber arrangement similar to that now in use but where scintillation counters were substituted for the spark chambers of the ECS[1]). The photon detection efficiencies for 2-spark (2-coun-ter) detection was ~85% above ~250 MeV decreasing to ~40% at 100 MeV.

Each of the four sets of chambers comprising the ESC system consist of ten cylindrical bigap spark chambers with aluminium plates interleaved with iron lead plates. (C$'_3$ has an additional quad-rigaps chamber). The capacity of each bigap ranges
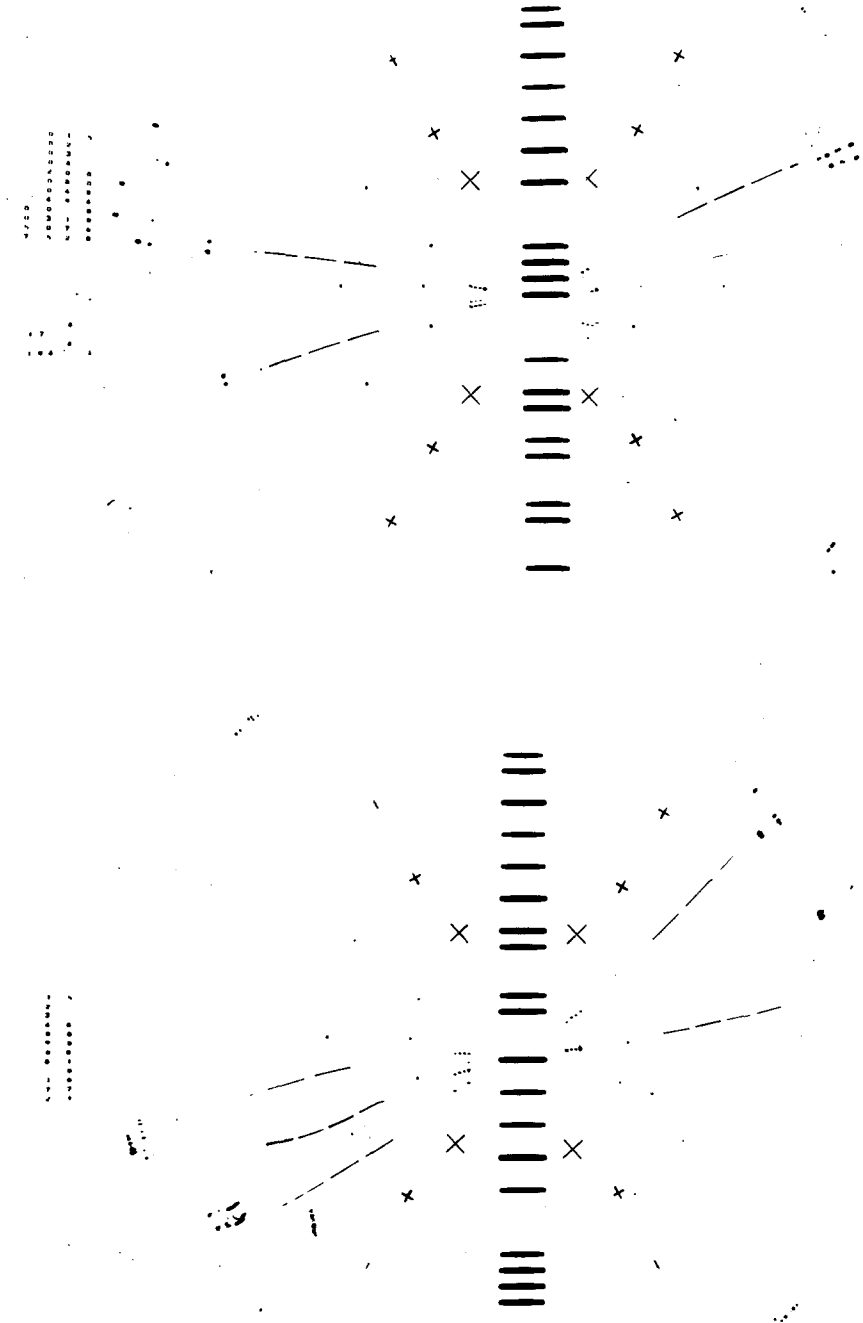
Fig. 13. Pictures of two typical multihadron events.

from 3000 pF for the inner bigap to 4500 pF for the outer. The high-voltage pulses from 8 spark-gap pulsers (each of output capacity of 20 nF) are applied, via coaxial cables, to each bigap. In order to minimize instabilities in this system, one hv trigger pulse was used to activate the 8 spark-gap pulsers. The recovery time for the whole system of 48 spark chambers was about 0.5 s. These chambers are operated with Henogal 30 (30% neon and 70% helium) and with a spark-gap charging a voltage of 10–11 kV. Under these conditions few spurious tracks are observed and stable operation at high efficiency is maintained.

3.3. OPTICAL SYSTEM OF THE APPARATUS

A side view of the apparatus with the optical system used to record events is shown in fig. 12. The images of the internal spark chambers C_2, C_2', are viewed by two 70 mm cameras with optic axes aligned with the magnet axis. With these two photographs the whole sensitive volume is visible. The camera lenses have focal lengths of 40 mm and are positioned 200 cm from the interaction region (at $x = \pm 200$ cm). Photographs are taken with 3M type 320 BW film and a lens setting of $f/8$. The maximum angular aperture used in photography is 60°.

In order to determine the position and angle of a wide-gap spark in space, the end points of each track in each gap must be measured on the film. With this measurement in only one view and from a knowledge of the camera position, of the optical axis position and of the cylindrical plate position, the spatial positions of the end points of each track are determined. Two cameras are necessary only because they permit a view of the full sensitive volume.

The narrow gap chambers C_1 and C_1' near the vacuum pipe are viewed by both cameras. As shown in fig. 12 the full view of these chamber gaps is possible through prisms at the ends of these chambers.

Half of the ESC are viewed by each camera. The stereoscopy for tracks in these chambers is achieved with a series of reflecting small-angle mirrors, RM in fig. 12, located at the far end from each camera. Track images from these chambers are brought in to the same picture as the internal chambers with parabolic (PR) and plane (PM) mirrors. The optical path length from the camera lenses to the center of each ESC is about 7 m. In fig. 12 a sketch of an event recorded on film is shown. The image size is 60×80 mm^2. In fig. 13, pictures of two typical multihadron events are shown.

3.4. MULTIWIRE PROPORTIONAL-COUNTER SYSTEM (MWPC)

Telescopes, each composed of two MWPC, were placed above and below the interaction region (see fig. 3). The sense wires are parallel to the direction of the beams thus allowing the direct geometrical reconstruction in the x–z plane of the interaction region. Each telescope contains $154 + 98 = 252$ sense wires spaced 2.5 mm apart. A "magic" gas mixture of 72% A, 23.5% isobutane, 0,5% Freon and 4% methylal vapor and an operating voltage of 4.7 kV are used. The effective thickness of each telescope is 0.76 g/cm^2 of fiberglass epoxy. The characteristics are summarized in table 3 and fig. 10.

The data collection system was divided into modules each containing 14 channels. A schematic diagram of the circuit used to amplify, store and
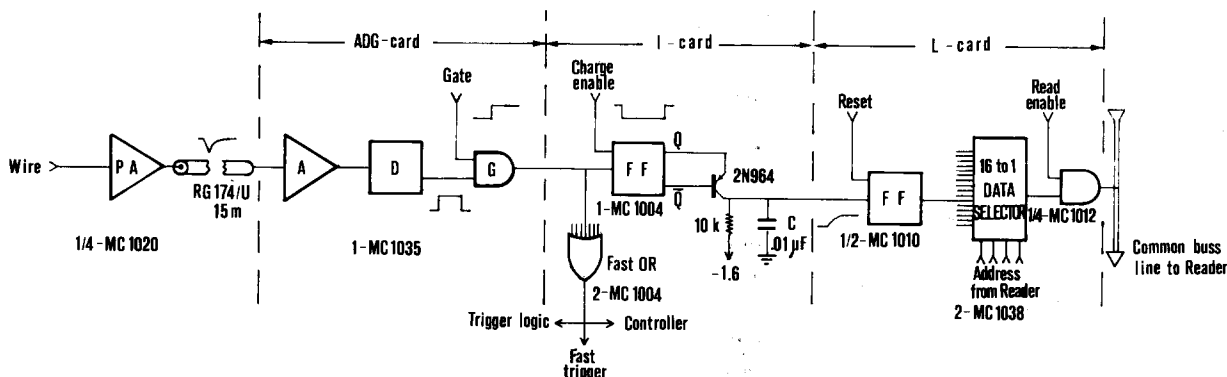
Fig. 14. Block diagram for a single MWPC channel containing preamplifier (PA), Amplifier-Discriminator-Gate (ADG), Integrator (I) and Latch (L) circuits.

register each sense wire signal is shown in fig. 14[9]). A preamplifier and cable driver, PA, were mounted on each chamber. After amplification to a MECL logic level in the Amplifier-Discriminator-Gate card (ADG) the signal is gated on to the Charge-Integration card (I) where, following a charge-enable coincidence signal, the storage capacitor (C) is charged. It is at this point in time that the wide-gap-chamber pulse occurs. With imperfect e-m shielding most circuits involved in amplifying and recording pulses are affected. The I-card and the Controller were carefully studied in order to assure that the charge on the capacitor, C, is unaltered by this disturbance. After this hv pulse subsides, the Latch card (L) is reset and the I-card capacitor discharged into the L-card flip flop. The wires are scanned by the Reader and the addresses of those with a charged capacitor are then transfered to the Laben 70 on-line computer.

In order to reduce the spurious trigger rates at Adone a first rough determination of the interaction point is used in the trigger logic. This was done with analog and not with digital circuits as good spark quality in the spark chambers requires the operation to be completed in $\leqslant 0.5\,\mu s$. The trigger logic is shown in schematic form in fig. 15. For each MWPC a priority encoder, PE, selects the extreme wire in the positive x direction and a digital-to-analog converter, DAC, provides a signal proportional to the position x of the trajectory of

the particle in both the internal and external MWPC's. A differential amplifier, DA, is strobed by a fast trigger formed by scintillation counters, and gives a signal which is proportional to the distance, S, of the trajectory from the projected beam position in the x–z plane. This output is analysed by a differential discriminator (DIF. DISC.) with a window set to select a maximum value for $|S|$. These logic operations are realized in a time of ~ 400 ns. The width of the discriminator and the logic pulses are chosen to select those events which have the trajectory of at least one particle within $|S| \lesssim 30$ mm. This requirement was found to reduce the overall trigger rate by a factor of $\sim 6.$

3.5. Trigger and data acquisition
3.5.1. Trigger counter system

In addition to the MWPC telescopes, the trigger counter system consists of four layers of scintillators. The first two layers (S_1, S_1' or S_2, S_2' in fig. 3) each with dimensions $35 \times 40 \times 0.5$ cm^3, were placed between the vacuum pipe and the first spark chamber ($C_1 C_1'$). The third (S_3, S_3') and fourth (S_4, S_4') layers, each with counter dimensions $200 \times 20 \times 2$ cm^3, were placed outside the main coil before the ESC (see fig. 3). Between S_3 and S_4 a 1.5 cm iron plate and between S_3' and S_4' a 0.5 cm lead plate were interposed to reduce the machine background at the higher energies of Adone. The external scintillators S_3 and S_3' are
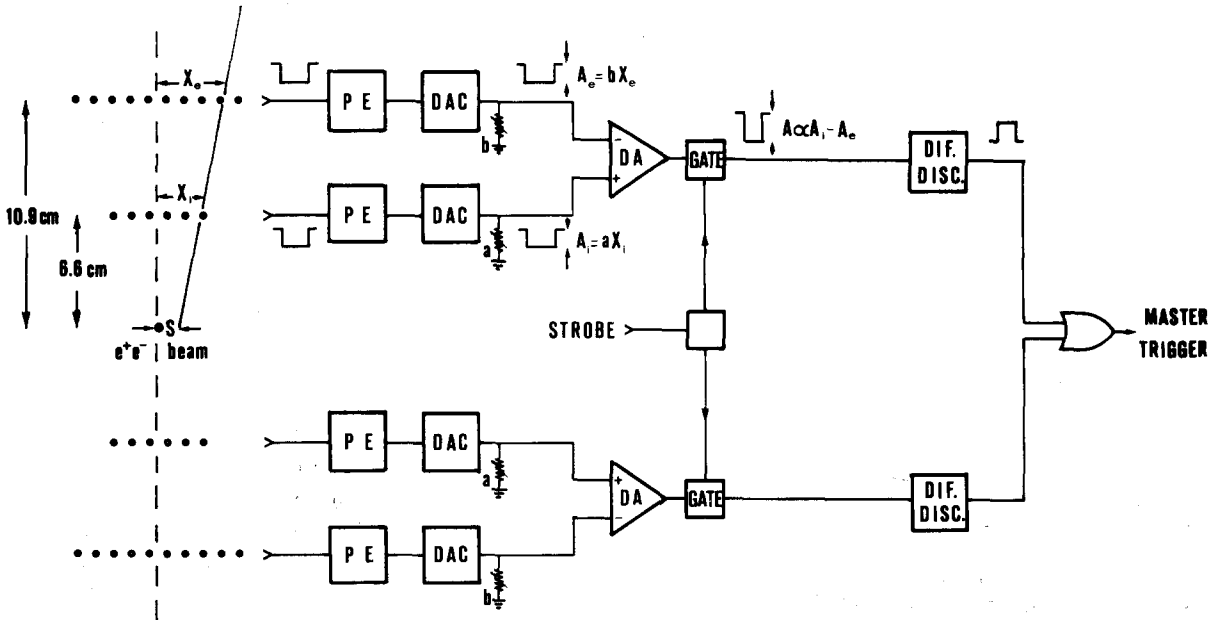
Fig. 15. Block diagram for MWPC trigger logic.

viewed from opposite ends by two photomultipliers, whereas for $S_1, S_1', S_2, S_2', S_4, S_4'$, only one PM tube is used for each. As seen in fig. 3, counter S_3, S_3', S_4, S_4' each subtends an angle from a point in the interaction region of $\sim 10°$. The minimum energy required for a pion to penetrate through to last scintillator layer (S_4, S_4') is 125 MeV and 100 MeV to penetrate through to the third layer (S_3, S_3').

The signals from both photomultiplier tubes in S_3 and S_3' are used to produce a position-independent timing signal employed in suppressing cosmic-ray triggers. Time measurements were made between S_1, S_2 and S_3 and between S_1', S_2' and S_3'. The time resolution as determined with $ee \rightarrow \mu\mu$ events at the J/ψ resonance is $\sigma = \pm 0.8$ ns with no angle correction, and $\sigma = \pm 0.6$ ns when corrected. Cosmic rays were rejected by setting the minimum time accepted by the upper counter system to 2–3 standard deviation (or 2–3 ns) from the electron peak for Bhabha scattering. As downward going cosmic rays would have a time difference of ~ 6 ns, they are rather effectively rejected, the rate being reduced to ~ 0.3 trigger/min.

3.5.2. The trigger configuration

The choice of a particular counter configuration for triggering the MEA detection system was con-
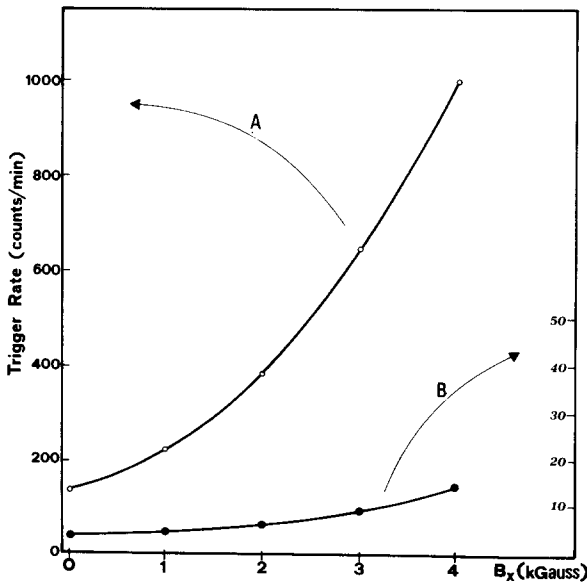
Fig. 16. Trigger rates vs MEA magnetic field, B_x, for two triggering conditions; (A) $(S_1 S_2 S_3) \cdot (S_1' S_2' S_3')$ and (B) master trigger described in the first part of section 3.5.2. Adone operation with 30 mA circulating (each beam) and $\sqrt{s} = 2.0$ GeV.

ditioned by several factors. In general, the trigger configuration chosen was required to be as "loose" and "soft" as possible but with a rate not to exceed 5 triggers per minute. This rate was set by the limited access for film change at Adone. Regarding the background rate due to cosmic rays, the application of the TOF criterion described above reduced this rate to a negligible value (~ 0.3 triggers/min). The major background was found to come from Adone itself. This background, which is beam correlated, is swept into the detection system by the MEA transverse magnetic field. At a particular Adone beam energy, the background rate was found to increase with increasing MEA magnetic field. This behaviour is seen in curve A of fig. 16, where the trigger rate for a particularly simple coincidence arrangement is plotted vs the magnetic field of MEA (B_x) with Adone operating normally at $\sqrt{s} = 2.0$ GeV and 30 mA per beam. A more complex master-trigger configuration employing MWPC (described below) was used to reduce these rates to the level seen in curve B of fig. 16. Based on this latter curve it was decided to limit the magnetic field of MEA to $B_x = 2.0$–2.5 kG depending on the e^+e^- beam energy.

The master trigger conditions that are used in data taking at energies $\sqrt{s} \leqslant 2.0$ GeV are the following:

a) time of flight between the inner counters, S_1, and the first layer of the external scintillators, S_3, set to exclude cosmic-ray events (as previously mentioned),

b) coincidence of the event occurence with that of the bunch-bunch crossing time in the interaction region, to within ± 3 ns,

c) correct source point for one track as determined by one of the MWPC telescopes (description in section 3.4),

d) coincidences of upper telescope $(S_1 S_2 S_3)$ and lower telescope $(S_1' S_2' S_3')$ (minimum pion energy for traversal ~ 100 MeV),

e) event rejection if only two tracks detected as $(S_1 S_2 S_3)$ and $(S_1' S_2' S_3')$ and if both tracks are either forward or backward within $\theta = 20°$–60° (ref. 10).

With these trigger requirements the cosmic-ray trigger rate was 0.3 triggers/min. With the MEA magnetic field at 3.0 kG and Adone operating at $\sqrt{s} = 1.6$ GeV, the total trigger rate increased to 4 triggers/min and at $\sqrt{s} = 2.0$ GeV to a value of 10 triggers/min.

It was at this point that further efforts were

made to "harden" the trigger requirements. Absorber layers of 1.5 cm of iron or 0.5 cm of lead and an additional ring of counters (S_4, S_4') were added. This final arrangement is that shown in fig. 3. Penetration of particles out to S_4 and S_4' could then be used to reduce the trigger rate. Penetration out S_4 or S_4' requires a pion energy of 125 MeV.

For operation at higher energies above $\sqrt{s} = 2$ GeV at Adone the above trigger conditions (d) and (e) were altered replacing the three-fold coincidences $(S_1 S_2 S_3)$ and $(S_1' S_2' S_3')$ by the four-fold coincidences $(S_1 S_2 S_3 S_4)$ and $(S_1' S_2' S_3' S_4')$ [11]), respectively. Also the following additional trigger coincidence conditions were added, in OR, to those described above:

f) coincidence for three tracks, two of which are tracks as specified in e) and the third as either $(S_1 S_2 S_3)$ or $(S_1' S_2' S_3')$,

g) gamma-ray trigger defined as having two penetrating tracks out to S_4 or S_4' both in the upper or lower telescope and, in the opposite telescope, one counter in either layer S_3 or S_4.

With $B_x = 3.0$ kG the trigger rate at $\sqrt{s} = 2.0$ GeV with the "harder" trigger specified above was 3 triggers/min and at 3.0 GeV, 5 triggers/min. The addition of g) as a trigger condition allows for the detection of $\omega^0 \pi^0$-like final states while increasing the trigger rate only by 30%.

For operation of MEA at $\sqrt{s} \leqslant 2.0$ GeV several less restrictive trigger combinations involving S_3, S_3', S_4 and S_4' have been used successfully.

3.5.3. On-line data acquisition

A Laben 70 mini-computer with a 20k memory and a disk operating system is used to record data and to perform certain control checks on apparatus operation. Data acquisition is through an on-line CAMAC system which is used to record for each event: the machine energy, the trigger configuration, the counters involved, the pulse-height sum in quadrants of counters $S_3 S_3'$, the MWPC wires which were registered, the times of flight in the upper and lower parts of the apparatus, and the relative time of the rf-signal. Part of this information including the frame number is optically displayed through nixies and recorded on film with each event. After the occurence of each event, a dead time of ~ 2 s is necessary for film advance. During this time the computer performs a check for satisfactory operation of the apparatus through the collection and analysis of cosmic-ray data; e.g. time

of flight, pulse height for each scintillation counter, and each MPWC wire address. Machine-produced events are written out on magnetic tape as they occur, cosmic-ray-summary data is registered every 15 min, and, at the end of a run, summary data distributions are recorded. The electronic data for each event can be displayed by the computer as well as the accumulated cosmic-ray or machine-event distributions.

3.5.4. Acceptance of the apparatus

The single-track acceptance of the apparatus in ϑ and φ is shown in fig. 17. In this figure the areas are proportional to the solid angle covered to midchamber by a point like source. Using this figure the solid angles of the various parts of the apparatus can be deduced. The solid angle covered by spark chambers $C_1 C_1'$ is $\Delta\Omega_{C_1 C_1'} = 0.56 \times 4\pi$ sr for a point source. The charged multiplicity of events is recorded in this solid angle. The momentum analysis, made in $(C_2 C_2')$, is possible over the solid angle of $\Delta\Omega_c = 0.35 \times 4\pi$ sr for a point source and $\Delta\Omega_c = 0.25 \times 4\pi$ sr for a source with $\sigma = \pm 17.0$ cm (at $\sqrt{s} = 2.0$ GeV). The solid angle useful for a particle identification (as defined by the chambers C_3, C_3') is $\Delta\Omega_N = 0.26 \times 4\pi$ sr for a point source and $\Delta\Omega_N = 0.18 \times 4\pi$ sr for a source with $\sigma = \pm 17.0$ cm (at $\sqrt{s} = 2.0$ GeV).
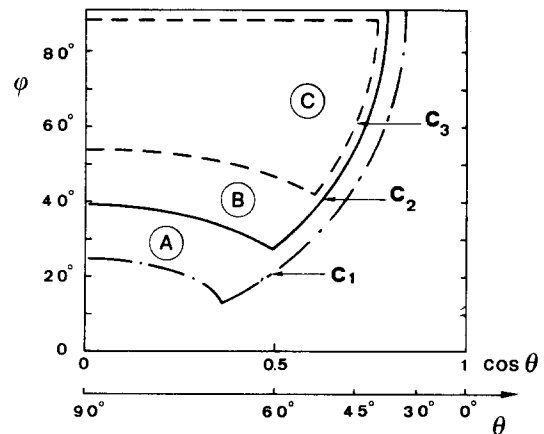
Fig. 17. Conformal representation of apparatus acceptance in ϑ–φ plane (see fig. 2). Acceptance is calculated to midchamber from a point source at $(0, 0, 0)$. The dash–dotted line defines the boundary of the area A, covered by $C_1 C_1'$, useful for charged multiplicity measurement; the full line delineates the region B covered by $C_2 C_2'$, useful for momentum analysis; the broken line delineates the region C covered by $C_3 C_3'$, useful for particle identification. Only $0 < \phi < 90°$ region represented.

4. Spatial reconstruction of spark chamber tracks and particle momentum determination

The optical system used to photograph the spark-chamber detectors of MEA is shown in fig. 12 and is described in section 3.3. The principal reason for employing two cameras was to be able to view the full volume of wide-gap cylindrical chambers.

Each view is analyzed separately using information on the positions of its own set of reference fiducials and of the wide-gap cylindrical plates and narrow-gap spark chambers. (MWPC measurements of track positions parallel to the magnetic field axis have yet to be introduced into the track reconstruction.) The reconstruction procedure used is non-standard and is specialized to the MEA geometry.

The coordinate system used in reconstruction is specified in fig. 2. In each view the coordinates of a point in space (x, y, z) are related to the points on the film, measured in rectangular coordinates (ξ, η), by the following relations:

$$\xi = \frac{C_1 x + C_2 y + C_3 z + C_4}{C_9 x + C_{10} y + C_{11} z + 1},$$

$$\eta = \frac{C_5 x + C_6 y + C_7 z + C_8}{C_9 x + C_{10} y + C_{11} z + 1},$$

(4)

where the coefficients $C_1 \dots C_{11}$ are determined from a fit of fiducial measurement on the film to the known positions in space of the fiducials. With the equations (4) a single point measured on the film specifies a straight line in space through the lens optical center. This line will be referred to as the "optical line". Consider now a segment of a wide-gap chamber track. The end points of this segment should lie on, or very near, the two cylindrical wire plates of the chamber gap. The space position of an end point then is determined as the point of intersection of the optical line with the cylinder specifying the position of the particular wide-gap chamber plate.

Three additional points along each track segment between end points also are measured. These are called internal points and are spatially reconstructed using the following procedure. First, the end-points of all gaps are fitted to a straight line in a plane $x–z'$, where z' is an axis approximately passing through the points of the track projected on to the $y–z$ plane. This best-fit line then is used to determine the x coordinate of the internal points from the points of intersection of this line with the projections of each optical line in the $x–z'$ plane. This straight-line dependence in x was assumed as the main component of the magnetic field is along x, and it has been found to introduce no significant error in momentum measurements.

An important effect that was considered and corrected for, is the displacement of the sparks during their formation due to E and $E \times B$ forces. In the wide-gap chambers the average magnitude of the displacement along E is 4.2 mm. The $E \times B$ displacement was found to be much smaller and was ignored. The correction is made by shifting each measurement of spark position along the electric field at that point, by this average displacement.

For the wide-gap chambers, the overall relative precision in the $y–z$ plane for a single measurement of the track position, including measurement errors, was found to be $\sigma = \pm 0.25$ mm [12]. The absolute error in determining the x position of a track was $\sigma_x = \pm 3.0$ mm. In the $y–z$ plane then the momentum error is $\Delta p/p = \pm 0.14$ at $p = 1.0$ GeV/c and with $B_x = 2.5$ kG and the error in the angle measurement (ψ in fig. 2) is $\sigma_\psi = \pm 1.0°$. The error in the depth angle measurement δ is $\sigma_\delta = \pm 1.5°$.

A similar procedure was used for the reconstruction of space points from film measurements made on sparks in the narrow-gap chambers (C_1, C_1' of fig. 3). Each measured point on the film determines an optical line. This line however is deviated by entrance prisms to lie in a plane parallel to the narrow-gap-chamber plates. In order to determine the x coordinate of a spark, a best-fit line to all wide-gap points in the plane $x–z'$ as described above was used. The x position along the deviated optical line was determined as the point of intersection of this best-fit wide-gap chamber line with the projection of the optical line on the $x–z'$ plane.

The precision alignment of the narrow-gap chambers was made using cosmic-ray muon tracks recorded with no magnetic field. A minimization procedure established the relative wide-gap narrow-gap position [13]. The most sensitive parameter that is determined in the fitting, is the vertical position (z) of each gap. Also given in this analysis is the precision of particle-position determinations from spark measurements made on narrow-gap chamber sparks. In the $y–z$ plane the relative pre-

cision per spark was $\sigma = \pm 1.0$ mm and the absolute error in x was $\sigma_x = \pm 10$ mm.

The resulting overall precision for the determination of the particle momenta in the y–z plane from measurements in the wide and narrow-gap chambers was found to be $\Delta p/p = \pm 0.07$ at $p = 1$ GeV/c and and $B_x = 2.5$ kG with an error in the angle measurement in this plane of $\sigma_\psi = \pm 0.5^0$. The error in depth angle determination remains unaltered at $\sigma_\delta = \pm 1.5°$. These values have been verified through measurements made on QED events of the type $e^+ e^- \rightarrow \mu^+ \mu^-$.

We would like to acknowledge the many important contributions of the Adone accelerator group in the design and operation of MEA at Adone and, in particular, Prof. F. Amman, Prof. M. Bassetti, Ing. A. Cattoni, Dr. M. Placidi and Prof. S. Tazzari. We would also like to thank the Frascati magnetic group for their aid in the realization of the MEA magnet. For the construction of the detectors we are grateful for the excellent work of the Frascati workshop directed by Messrs. G. Di Stefano and R. Bonini and also of the workshops of Padova, Pavia and Maryland Universities.

Finally, we would like to express our appreciation to Messrs. G. Schina and R. Giantin for indispensable technical assistance throughout the construction and operation of this apparatus.

References

[1] W. Ash, D. Grossman, G. Mattiae, G. P. Murtas, M. Nigro, G. K. O'Neill, G. Sacerdoti, R. Santangelo, D. Scannicchio and E. Schiavuta, Laboratori Nazionali Frascati, Internal Report LNF-69/2 (1969).

[2] F. Amman, Memorandum ADONE, ME-27 (1969).

[3] A. Cattoni, M. Piccolo and F. Ronga, Nucl. Instr. and Meth. 96 (1974) 573.

[4] M. Placidi, F. Soso and M. Vescovi, Laboratori Nazionali Frascati, Internal Report LNF-68/30 (1968).

[5] H. Ogren, A. Marini and D. Bisello, Laboratori Nazionali Frascati, Internal Report LNF-73/59 (1973).

[6] W. W. Ash, P. Monacelli, M. Piccolo and F. Ronga, Laboratori Nazionali Frascati, Internal Report LNF-73/26 (1973).

[7] W. W. Ash and D. Bisello, Laboratori Nazionali Frascati, Internal Report LNF 70/2 (1970).

[8] D. Bisello and F. Ronga, Laboratori Nazionali Frascati, Internal Report LNF-70/44 (1970).

[9] A description of the ADG, L, and Reader circuits is given in M. Cavalli–Sforza and D. C. Cheng, Nucl. Instr. and Meth. 113 (1973) 81.

[10] At energies below $\sqrt{s} = 2$ GeV, three track events were not rejected if one of the tracks appeared outside this angular interval and penetrated out to S_3 or S_3'.

[11] The actual coincidences used in the trigger were more complex, i.e. $\sum_i S_1 \cdot S_2 [(S_{3_i} \cdot S_{4_{i+1}}) + (S_{3_i} \cdot S_{4_i})]$ and $\sum_i S_1' \cdot S_2' \cdot [(S_{3_i}' \cdot S_{4_{i+1}}') + (S_{3_i}' \cdot S_{4_i}')]$.

[12] This error does not represent the minimum or intrinsic error that characterizes these wide-gap chambers. It represents the best value of the error for measurements made on a 0.6× full-size projection of the central-chamber image with a mangiaspago digitizer having a least count of 33 μm.

[13] We would like to thank Drs. S. D'Angelo and R. Bernabei for having developed this minimization procedure.